RSC Advances

PAPER

View Article Online
View Journal | View Issue

Cite this: *RSC Adv.*, 2025, **15**, 44623

Interrelated lithium-ion transport, NTCR behavior, and dielectric-optical coupling in multifunctional $Li_3Mg_2NbO_6$ ceramic

Samia Aydi, [a] Mohamed Mounir Bouzayani, [a] Moufida Boukriba,[b] Saber Nasri, [a] Omar Radhi Alzoubi[c] and Abderrazek Oueslati *[a]

The rapid progress of 5G/6G communication and advanced radar systems demands dielectric ceramics with excellent microwave performance and multifunctional characteristics. Lithium-based $Li_3Mg_2NbO_6$ (LMN), crystallizing in a rock-salt-derived orthorhombic structure, is identified as a promising candidate due to its structural stability and tunable dielectric response. LMN ceramics were synthesized by the solid-state route and comprehensively analyzed using X-ray diffraction, UV-Vis spectroscopy, and impedance spectroscopy. The material exhibits a direct bandgap of 3.78 eV, indicating potential for optoelectronic and photocatalytic applications, while an Urbach energy of 0.92 eV reveals structural disorder affecting charge transport. Impedance results confirm thermally activated hopping conduction with an activation energy of 1.16 eV, governed by non-Debye relaxation associated with defect-mediated mechanisms. The strong correlation between structure, optical properties, and charge dynamics highlights LMN as a versatile, high-performance ceramic for next-generation microwave and UV-responsive electronic devices.

Received 6th September 2025
Accepted 28th October 2025

DOI: 10.1039/d5ra06717k

rsc.li/rsc-advances

1. Introduction

The rapid development of next-generation wireless technologies, including 5G/6G networks, satellite communications, and radar systems, has intensified the search for advanced dielectric ceramics capable of sustaining high-frequency operation with minimal energy dissipation.[1–3] Within this context, lithium-based ceramics have emerged as promising candidates due to their chemical stability, low production cost, and environmental compatibility.[4–8] Their multifunctional character combining structural robustness with excellent dielectric and thermal properties has positioned them at the forefront of materials research for microwave and electronic applications.[9–13]

A particularly important subgroup of these ceramics comprises lithium-containing compounds with rock-salt-derived structures, which exhibit tunable permittivity, low dielectric losses, and remarkable thermal stability.[14–18] Beyond their established microwave performance, these materials have demonstrated unique functionalities, such as the Negative Temperature Coefficient of Resistance (NTCR) effect, making them attractive for thermistor applications.[19,20] Their structural flexibility has also stimulated interest in energy storage and optoelectronic devices, broadening their technological relevance. Representative compounds including $Li_2Mg_3TiO_6$, Li_2MgTiO_4, $Li_2Mg_4TiO_7$, and $Li_3Mg_2NbO_6$ have consistently shown excellent dielectric performance, enabling their use in resonators, filters, and antennas essential for modern communication systems.[21–27]

Among these, $Li_3Mg_2NbO_6$ (LMN) has attracted particular attention owing to its distinctive orthorhombic structure derived from rock-salt supercells.[28] In this lattice, Nb^{5+} occupies well-defined octahedral sites within a close-packed oxygen framework, while Li^+ and Mg^{2+} ions share multiple octahedral positions in a partially ordered arrangement.[33–35] This ordering results in distorted [$Li/Mg/NbO_6$] octahedra, which strongly influence the dielectric, thermal, and functional properties of the material.[36] Recent studies, have advanced the understanding of LMN's structural evolution and microwave dielectric response, employing spectroscopic techniques to link cation ordering with dielectric behavior.[29–32] In the case of $Li_3Mg_2NbO_6$ (LMN), the term "8a Wyckoff position" refers to the specific cation site within its ordered double perovskite-type structure. The compound crystallizes in the orthorhombic system with the *Fddd* (no. 70) space group, typical of rock-salt-derived ordered perovskites. In this crystal structure, Li^+ ions primarily occupy the 8a Wyckoff sites, while Mg^{2+} and Nb^{5+} ions are distributed over the 4c and 4d positions, respectively.

[a]*Laboratory of Spectroscopic and Optical Characterization of Materials (LaSCOM), Faculty of Sciences, University of Sfax, B. P. 1171, 3000 Sfax, Tunisia. E-mail: oueslatiabderrazek@yahoo.fr*

[b]*Department of Chemistry, College of Science, Qassim University, Buraydah 51452, Saudi Arabia*

[c]*Computing Department, College of Engineering and Computing in Al-Qunfudah, Umm Al-Qura University, Kingdom of Saudi Arabia*

Oxygen atoms are located at the 8d sites, completing the framework of corner-shared [MgO_6]/[NbO_6] octahedra. These atomic distributions are consistent with our Rietveld refinement results and previously reported literature on similar complex oxides.[33–36] To assess $Li_3Mg_2NbO_6$ as an advanced dielectric ceramic, it is crucial to link its intrinsic properties to performance. Its orthorhombic structure and ordered cation distribution enhance polarizability and reduce dielectric loss, while the wide bandgap and controlled defect states limit electronic conduction pathways. Temperature-dependent electrical behavior further ensures thermal stability. Together, these factors justify the comprehensive study of structural, optical, and electrical properties to optimize LMN for high-performance dielectric applications.

Despite this progress, important aspects of LMN remain underexplored. In particular, its charge transport mechanisms, relaxation dynamics, and optical properties have not been fully clarified, even though these factors are critical for tailoring multifunctional ceramics for energy-efficient microwave and electronic applications. Addressing this knowledge gap, the present study provides a systematic investigation of LMN's crystal structure, optical behavior, and frequency- and temperature-dependent electrical transport properties. By correlating intrinsic structural features with charge carrier dynamics, we deliver insights into how lattice distortions and cation distribution govern relaxation processes. These findings not only deepen the scientific understanding of LMN but also highlight its potential as a multifunctional platform material for next-generation dielectric and electronic devices.

2. Experimental section

2.1. Sample preparation of $Li_3Mg_2NbO_6$

$Li_3Mg_2NbO_6$ was synthesized *via* a conventional solid-state reaction route. High-purity starting powders lithium carbonate (Li_2CO_3, 99%, Sigma-Aldrich), magnesium oxide (MgO, 99%, Sigma-Aldrich), and niobium oxide (Nb_2O_5, 99.9%, Sigma-Aldrich) were stoichiometrically weighed and homogenized by dry ball-milling in an agate mortar for 2 hours to ensure uniform mixing. The mixed powder was then calcined in an alumina crucible at 900 °C for 8 hours in a muffle furnace to decompose carbonates and initiate phase formation, with intermittent grinding to promote reactivity.

The calcined powder was re-milled for 1 hour to refine particle size and improve homogeneity, followed by uniaxial pressing into pellets (8 mm diameter, ~1 mm thickness) at 150 MPa. Finally, the pellets were sintered at 900 °C (1173 K) for 2 hours in air to achieve densification and crystallize the desired $Li_3Mg_2NbO_6$ phase. Phase purity and structural evolution were confirmed by X-ray diffraction (XRD), as shown in Fig. 1.

2.2. Materials characterisation

X-ray diffraction (XRD) analysis of $Li_3Mg_2NbO_6$ was performed using a Philips powder diffractometer with a Cu Kα radiation source ($\lambda \approx 1.54187$ Å), operating at 40 kV and 40 mA. Measurements were conducted at room temperature in Bragg–Brentano (θ–2θ) geometry, with a Ni filter to suppress Kβ radiation. The diffraction patterns, collected over a 2θ range of 10°–80° with a step size of 0.02°, were analyzed for phase identification, lattice parameters, crystallite size, and microstrain using peak fitting methods.

The optical measurements were conducted with a Shimadzu UV-3101PC spectrophotometer equipped with a 150 W xenon arc lamp as the excitation source. An excitation wavelength of 275 nm was selected, corresponding to the bandgap absorption edge of $Li_3Mg_2NbO_6$, to ensure efficient electron–hole pair generation and probe direct band-to-band transitions. Emission spectra were acquired across the 200–800 nm range using a high-sensitivity photomultiplier tube (PMT) detector, with a spectral resolution of 1 nm. To minimize interference from

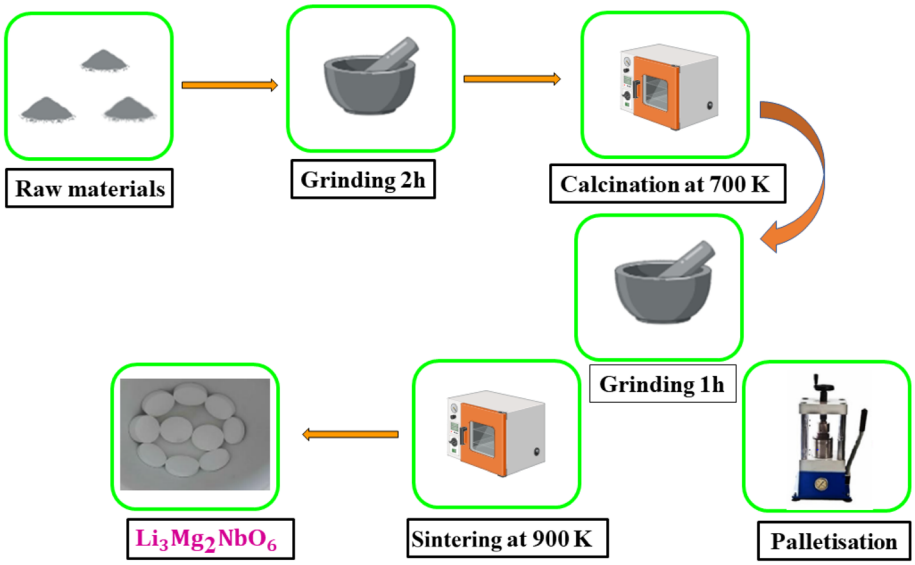

Fig. 1 Process flow chart for the solid-state synthesis of $Li_3Mg_2NbO_6$.

scattered excitation light, a long-pass optical filter was employed.

The electrical properties of $Li_3Mg_2NbO_6$ were analyzed by impedance spectroscopy using a Solartron 1260 Impedance Analyzer over a frequency range of 10 Hz to 5 MHz with an AC amplitude of 500 mV. Measurements were performed on a sintered pellet with silver electrodes, ensuring good electrical contact and minimizing electrode polarization effects. The temperature was varied from 493 K to 673 K using a controlled heating stage to investigate the temperature dependence of the electrical response.

Combined, these techniques provide a comprehensive understanding of the structural framework, optical characteristics, and electrical properties of $Li_3Mg_2NbO_6$. This multifaceted analysis enables a deeper evaluation of its fundamental behavior and supports its potential suitability for advanced functional applications in optoelectronic and energy-related technologies.

3. Results and discussion

3.1. X-ray diffraction analysis

The phase purity, crystal structure, and phase composition of $Li_3Mg_2NbO_6$ were characterized by X-ray diffraction (XRD). Fig. 2 presents the Rietveld-refined XRD pattern of the sintered ceramic, obtained at room temperature ($2\theta = 20°–80°$) using FullProf software.[37] The analysis confirms a pure orthorhombic phase (space group *Fddd*), consistent with the reference JCPDS file (#86-0346),[38] with no detectable secondary phases. The refined lattice parameters (Table 1) show excellent agreement with previously reported values,[39,40] validating the successful synthesis of phase-pure $Li_3Mg_2NbO_6$.

A detailed summary of the refined structural parameters obtained from the Rietveld refinement is presented in Table 1. The table includes the lattice constants, atomic coordinates (x, y, z), site occupancies, and reliability factors (R_{wp}, R_p, χ^2), as well as the calculated cell volume. These results provide a comprehensive overview of the crystallographic characteristics of LMN and confirm the successful fitting between the experimental and simulated XRD patterns, as shown in Fig. 2.

Table 1 Refined structural parameters of $Li_3Mg_2NbO_6$ obtained from Rietveld refinement of $Li_3Mg_2NbO_6$ at room temperature

Compound	$Li_3Mg_2NbO_6$					
Space group	*Fddd*					
Crystal system	Orthorhombic					
Unit cell dimensions						
a (Å)	8.552					
b (Å)	5.897					
c (Å)	17.721					
V (Å)	895.055					
R_p (%)	5.2					
R_{wp} (%)	6.8					
R_{exp} (%)	5.8					
χ^2	2.1					
D_{SC} (nm)	38					
δ (cm^{-2})	26×10^3					
Atom	Li(1)	Li(2)	Mg	Nb	O(1)	O(2)
Wyckoff site	4c	4c	4b	4a	4c	8d
x	0.250	0.750	0.500	0.000	0.250	0.489
y	0.250	0.250	0.000	0.000	0.038	0.250
z	0.000	0.500	0.000	0.000	0.250	0.756
Occupancy	1.0	1.0	1.0	1.0	1.0	1.0

X-ray diffraction (XRD) patterns were utilized to estimate the average crystallite size (D_{SC}) of the $Li_3Mg_2NbO_6$ sample. The crystallite size was calculated using the Debye–Scherrer equation, expressed as follows:[41]

$$D_{SC} = \frac{K\lambda}{\beta \cos\theta} \quad (1)$$

Here, β represents the full width at half maximum (FWHM) of the diffraction peak intensity, measured in radians. The dimensionless shape factor K is typically taken as 0.94. The wavelength of the Cu Kα radiation, λ, is 1.5406 Å, and θ denotes the Bragg angle corresponding to the diffraction peak.

Dislocation density (δ) is a key structural parameter that provides insight into the defect concentration within the sample. For $Li_3Mg_2NbO_6$ nanoparticles, the dislocation density was calculated using the relation:[42]

$$\delta = \frac{1}{D_{SC}^2} \quad (2)$$

The crystallite size and dislocation density values obtained *via* Scherrer's method, as summarized in Table 1, offer valuable information about the material's microstructure. Physically, these parameters reflect the average size of the crystalline domains and the degree of lattice distortion caused by defects or internal stresses. Notably, smaller crystallite sizes generally correspond to stronger materials due to their ability to hinder dislocation motion.

The density of polycrystalline $Li_3Mg_2NbO_6$ significantly influences its physical properties. The powder density $\rho_{X\text{-ray}}$ was determined from XRD data using the formula:[43]

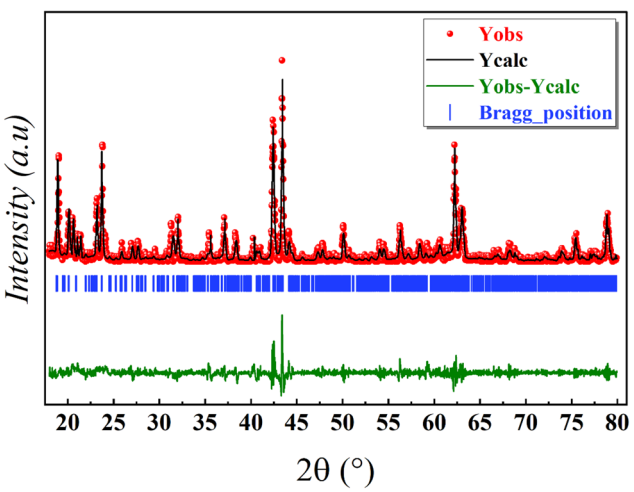

Fig. 2 Rietveld refinement profile carried out through FullProf software of $Li_3Mg_2NbO_6$.

$$\rho_{\text{X-ray}} = \frac{ZM}{VN_A} \quad (3)$$

where M is the molecular weight, N_A is Avogadro's number, V is the unit cell volume, and $Z = 4Z = 4$ is the number of formula units per unit cell. Using the following relations, the bulk density (ρ_{exp}), porosity (P), and specific surface area (S) were calculated according to eqn (4), (5), and (6):[44]

$$\rho_{exp} = \frac{m}{\pi r^2 h} \quad (4)$$

where r is the pellet radius, and h and m are the thickness and mass of the pellet, respectively. The capacity (C), representing the relative density of the sample, was calculated as:

$$C = \frac{\rho_{exp}}{\rho_{\text{X-ray}}} \quad (5)$$

Assuming spherical particles, the specific surface area was estimated using:

$$S = \frac{6000}{\rho_{exp} \times D_{SC}} \quad (6)$$

For the annealed sample, the lattice parameters obtained from Rietveld refinement yielded bulk and powder densities of 3.853 g cm^{-3} and 3.987 g cm^{-3}, respectively. The capacity and specific surface area were determined to be 0.966 and 38.543 m^2 g^{-1}, respectively.

In addition to the structural observations, the annealing temperature has a significant impact on the densification behavior of the material. Higher annealing temperatures enhance atomic mobility, facilitating diffusion along grain boundaries and lattice sites, which in turn promotes grain growth and reduces residual microstrain, as reflected by the sharper XRD peaks and decreased FWHM values. These structural improvements are physically associated with the elimination of lattice defects and pore shrinkage, leading to a more compact microstructure and improved densification. Consequently, the observed enhancement in crystallinity and reduction in microstrain indicate that thermal treatment provides the necessary energy to overcome diffusion barriers, thereby enabling the material to achieve higher packing density, which influenced in electrical study.[45,46]

3.2. Electrical properties

3.2.1. Impedance study. Complex Impedance Spectroscopy (IS) is a versatile technique used to study electrical transport, polarization, and charge relaxation in materials. It analyzes how low-resistance grains and high-resistance grain boundaries influence conductivity and dielectric behavior. By measuring impedance across a wide frequency and temperature range, IS distinguishes contributions from grains, boundaries, and electrodes, revealing charge transport, defect states, and thermally activated processes like ionic diffusion.[47–50] This study uses IS to investigate material transport properties, correlate electrical behavior with microstructure, and optimize materials for electronics, energy storage, and sensors.

Fig. 3(a) displays the temperature-dependent Nyquist plot ($-Z''$ *vs.* Z') for $Li_3Mg_2NbO_6$ between 493 K and 673 K. Unlike conventional dielectric materials that often show three distinct semicircular arcs corresponding to grain, grain boundary, and electrode interface effects,[51] our sample exhibits a single flattened semicircular response. This behavior suggests overlapping contributions from both bulk grain and grain boundary conduction mechanisms, with no detectable electrode polarization effects.

The observed semicircular arc becomes progressively smaller with increasing temperature, as seen by the reduction in both its diameter and real-axis intercept (Fig. 3(a)). This temperature-dependent evolution clearly demonstrates enhanced electrical conduction at elevated temperatures. To quantitatively analyze the overlapping grain and grain boundary contributions embedded within this single arc, we utilize the Maxwell–Wagner equivalent circuit approach,[52,53] which enables deconvolution of these competing conduction pathways. The spectra were successfully modeled using a two-cell circuit model, consisting of two parallel combinations (inset Fig. 3(a)).

Fig. 3(b) presents the frequency-dependent real impedance $Z'(\omega)$ for the $Li_3Mg_2NbO_6$ sample over a temperature range of 493–673 K, displaying a sigmoidal pattern. At lower frequencies, $Z'(\omega)$ exhibits higher values, which decrease with increasing frequency and temperature, aligning with a negative temperature coefficient of resistance.[54] This results in increased AC conductivity at elevated temperatures. At higher frequencies, the impact of grain boundaries on impedance weakens, with $Z'(\omega)$ converging across temperatures, possibly due to space charge release and diminished barrier effects, enhancing AC conductivity. The corresponding imaginary impedance (Z'') spectrum in Fig. 3(c) reveals temperature-dependent relaxation peaks that broaden and shift with heating. These peaks occur when the applied field frequency matches the characteristic hopping frequency of localized charge carriers. The observed peak broadening, which exceeds that predicted by ideal Debye relaxation, confirms non-Debye behavior in $Li_3Mg_2NbO_6$. Furthermore, the progressive peak widening with temperature reflects an increase in relaxation time distribution, demonstrating thermally activated charge carrier dynamics.

The temperature-dependent evolution of grain resistance (R_g) and grain boundary resistance (R_{gb}), derived from impedance spectroscopy (Fig. 3d and e), elucidates the interplay between microstructure and charge transport. Both R_g and R_{gb} decrease with rising temperature, albeit through distinct mechanisms. For R_g, the reduction stems from thermally activated charge carriers in grain interiors, where increased phonon-assisted hopping and diminished scattering losses enhance bulk conductivity.[55] Concurrently, R_{gb} declines due to the thermal lowering of potential barriers at grain boundaries, which mitigates space-charge effects and defect-mediated trapping. This dual reduction highlights a transition in conduction dominance: at low temperatures, grain boundaries govern transport through barrier-limited processes, while at elevated temperatures, intrinsic grain mobility prevails. The impedance spectra corroborate this behavior, with relaxation peak shifts reflecting accelerated carrier dynamics under heating. Collectively, these trends demonstrate how thermal energy

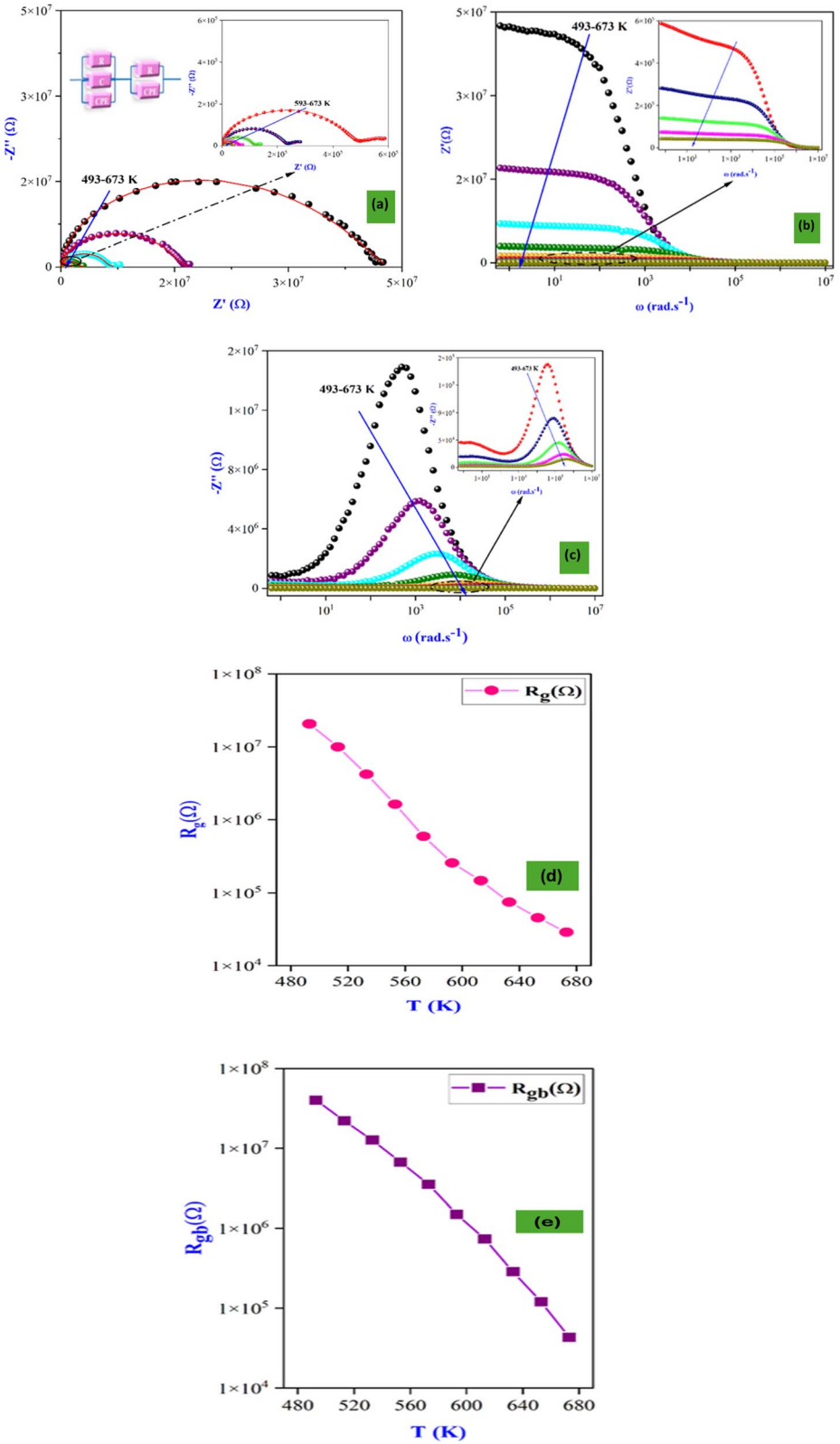

Fig. 3 Nyquist plots (a), the frequency dependence of the real part (Z') (b), imaginary part (Z'') of the complex electrical impedance (c), the dependence resistances of grain (R_g) (d) and grains (R_{gb}) at different temperatures of $Li_3Mg_2NbO_6$ (e).

modifies the material's energy landscape reducing resistive losses in both crystalline grains and disordered boundaries to optimize overall charge transport.[56]

The temperature-dependent impedance spectra were recorded over the range of 493–673 K, chosen to probe the intrinsic electrical response of $Li_3Mg_2NbO_6$ under conditions of

enhanced ionic mobility while maintaining structural stability. Within this temperature window, the material exhibits thermally activated conduction and polarization processes, as reflected in the evolution of the Nyquist plots (Fig. 3). This range provides a comprehensive understanding of the relaxation mechanisms and allows for consistent comparison with other temperature-dependent measurements, including dielectric and conductivity analyses. The observed trends confirm that the conduction and relaxation phenomena are strongly influenced by temperature, highlighting the role of thermally activated charge carriers in LMN.

3.2.2. Complex conductivity spectroscopy. In disordered solids, electrical conductivity stems primarily from charge carriers hopping between localized sites, driven by thermal activation and the applied electric field, shaping both DC and AC conductivity.[57] As depicted in Fig. 4, which illustrates conductivity trends, AC conductivity varies with temperature and frequency. At low frequencies, DC contributions dominate, showing minimal dispersion as ions complete long-range hops. At higher frequencies, AC conductivity prevails due to rapid charge carrier responses to the oscillating field, causing significant dispersion. The Jump Relaxation Model (J. Werking model)[58] elucidates this: at low frequencies, ions achieve successful long-range hops; at intermediate frequencies, reversible (unsuccessful) hops introduce dispersion; and at very high frequencies, successful hops regain dominance. This frequency dependence is quantitatively captured by Jonscher's universal power law:[59]

$$\sigma_{ac}(\omega, T) = \sigma_{dc}(T) + A\omega^{s} \quad (7)$$

where $\sigma_{dc}(T)$ represents DC conduction from long-range motion, and $A\omega^{s}$ describes dispersive AC conductivity. The exponent s ($0 \leq s \leq 1$) reflects charge carrier-lattice coupling strength, with $s \approx 1$ indicating weak interactions and $s < 1$ denoting stronger coupling.[60,61]

Arrhenius analysis of the DC conductivity (Fig. 5) yields an activation energy $E_a = 1.16 \pm 0.03$ eV for $Li_3Mg_2NbO_6$, consistent with efficient Li^+ migration in rock-salt structured ceramics.

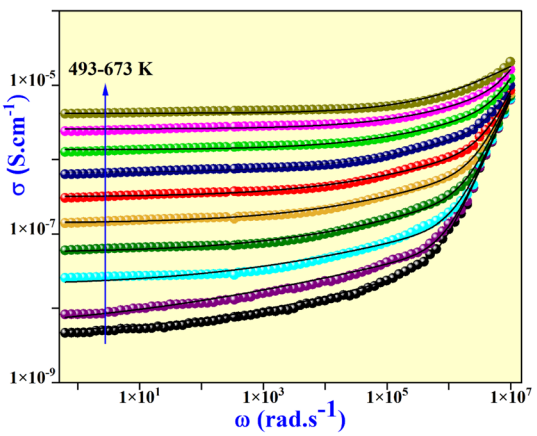

Fig. 4 The variation of (σ) *versus* (ω) at different temperatures of $Li_3Mg_2NbO_6$.

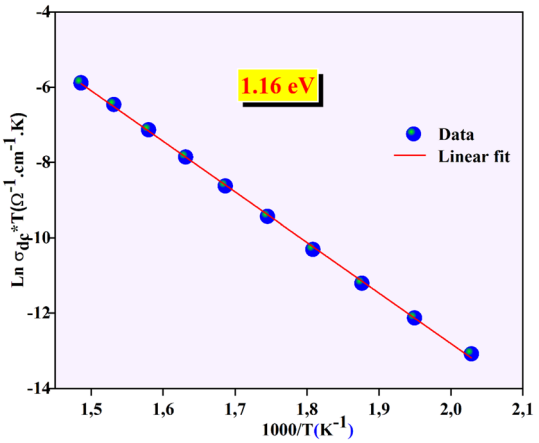

Fig. 5 Evolution of $\ln(\sigma_{dc}T)$ as a function of $(1000/T)$.

Investigating the mechanisms of charge transport in $Li_3Mg_2NbO_6$, materials is essential for understanding their electrical characteristics. The temperature-related changes in the exponent s offer key insights into the primary conduction pathways. Various theoretical frameworks have been developed to account for the behavior of s, often integrating quantum mechanical tunneling with charge carrier hopping. In these frameworks, particles such as electrons, polarons, or ions overcome energy barriers, providing clarity on the fundamental conduction processes.

One such model, overlapping large polaron tunneling (OLPT), characterizes the movement of large polarons, where significant overlap between adjacent potential wells facilitates efficient charge transfer. In contrast, non-overlapping small-polaron tunneling (NSPT) describes charge transport *via* small polarons hopping between isolated states with limited overlap. Another framework, correlated barrier hopping (CBH), depicts conduction as charge carriers moving between localized sites, influenced by Coulomb interactions and energy barriers. Additionally, pure quantum mechanical tunneling (QMT) explains charge carriers passing through barriers without requiring thermal activation.[62–65]

Analyzing the temperature dependence of the exponent s enables researchers to determine the most appropriate model for describing charge transport in $Li_3Mg_2NbO_6$, materials. This study not only deepens our understanding of conduction mechanisms but also supports the optimization of material properties for targeted applications, such as energy storage, solid-state batteries, and advanced electronic devices.

Fig. 6 depicts the temperature-dependent variation of s, showing an initial decrease followed by a slight increase at higher temperatures. This pattern aligns with the Non-Overlapping Small Polaron Tunneling (NSPT) model, which describes charge transport as thermally assisted tunneling of polarons (localized carriers coupled with lattice distortions) between defect centers.

The NSPT model predicts the following relation for $s(T)$:

$$s(T) = 1 - \left(\frac{4}{\ln\left(\frac{1}{\omega\tau_0}\right) - \frac{W_H}{k_B T}} \right) \quad (8)$$

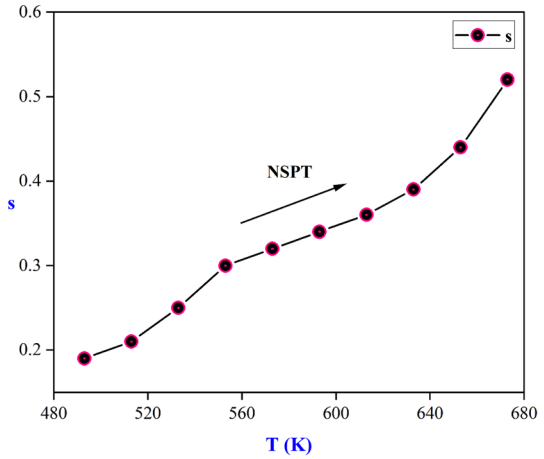

Fig. 6 Temperature dependence of the exponent "*s*" of $Li_3Mg_2NbO_6$.

where W_H is the polaron hopping energy and τ_0 is a characteristic relaxation time which is in the order of an atom vibrational period $\tau_0 \approx 10^{-13}$ s.[63] The AC conductivity can also be described microscopically using the expression:

$$\sigma_{ac} = \frac{(\pi e)^2 k_B T \alpha^{-1} \omega [N]^2 R_\omega^4}{12} \quad (9)$$

Whither

$$R_\omega = \frac{1}{2\alpha}\left[\ln\left(\frac{1}{\omega\tau_0}\right) - \frac{1}{k_B T}\right] \quad (10)$$

This formulation ties the frequency dependence of AC conductivity to fundamental polaronic parameters, offering a microscopic understanding of the conduction process.

The variation of AC conductivity as a function of temperature at various frequencies is shown in Fig. 7. These curves confirm the thermally activated nature of the charge transport and support the validity of the NSPT model in describing the behavior of $Li_3Mg_2NbO_6$ over the studied temperature and frequency ranges.[66–69] The fitting parameters are summarized in Table 2.

This model not only explains the frequency and temperature dependence of AC conductivity but also quantitatively links microscopic polaronic parameters such as hopping energy (W_H), lattice relaxation time (τ_0), and defect spacing to

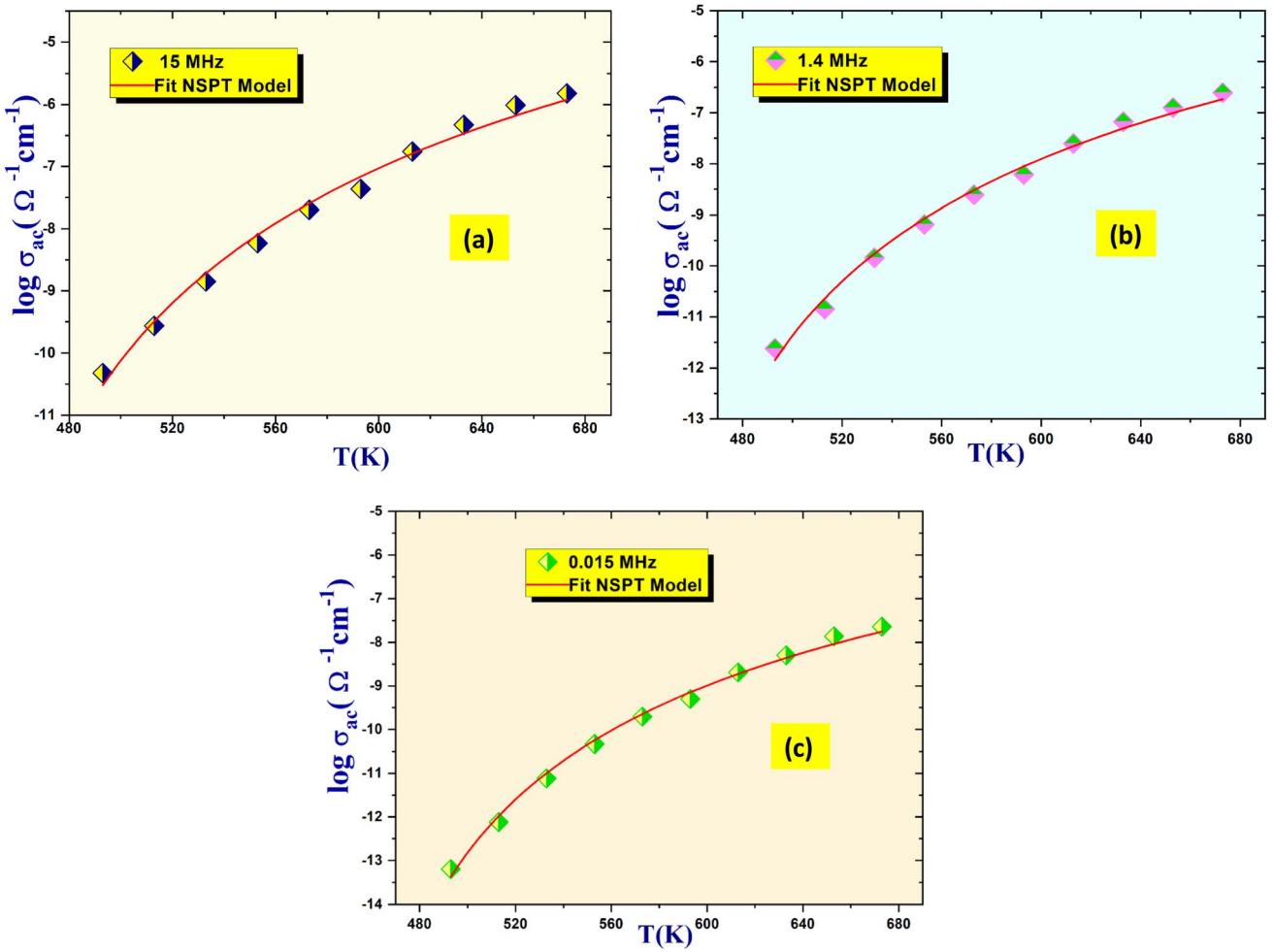

Fig. 7 (a–c) Graphs of ln σ_{ac} *versus* 1000/*T* for $Li_3Mg_2NbO_6$ at specific frequencies.

Table 2 AC conductivity parameters at various frequencies

	Frequency (MHz)	W_H (eV)	ε'	N (eV^{-1} cm^{-1})	α ($Å^{-1}$)
NSPT model	0.15	0.28	0.46	2.9×10^{17}	0.43
	1.4	0.27		4.8×10^{18}	0.51
	15	0.18		5.1×10^{19}	0.56

macroscopic electrical behavior. For instance, W_H, derived from the temperature-dependent exponent s, reflects the energy required to dissociate a charge carrier from its lattice distortion, while $\tau_0 \sim 10^{-13}$ s corresponds to the atomic vibration timescale governing polaron dynamics. These insights enable predictive material optimization: reducing W_H (*via* oxygen vacancies or cation substitution) could enhance ionic mobility, while tuning defect spacing may minimize hopping losses at intermediate frequencies. In $Li_3Mg_2NbO_6$, the rock-salt framework facilitates small polaron migration by balancing disorder with lattice flexibility, offering practical guidance for solid-state batteries (*e.g.*, designing low-barrier Li^+ pathways) and high-frequency electronics (*e.g.*, doping-engineered conductivity control). By connecting atomic-scale polaronic effects to bulk conductivity, this framework accelerates the development of advanced energy storage and electronic devices.

3.2.3. Dielectric measurements. Dielectric relaxation offers essential insights into charge dynamics, polarization mechanisms, and energy losses in materials exposed to alternating electric fields, aiding applications from energy storage to high-frequency devices. By studying dielectric properties, researchers can explore the connection between charge conduction and energy dissipation, critical for material performance. The complex permittivity, $\varepsilon^*(\omega) = \varepsilon'(\omega) - i\varepsilon''(\omega)$, underpins this analysis: $\varepsilon'(\omega)$ reflects the material's capacity to store energy *via* dipole orientation and ionic/electronic polarization,[70] while $\varepsilon''(\omega)$ indicates energy losses due to resistive effects from charge movement or dipole realignment.[71]

The dielectric constant (ε') of the material exhibited significant temperature (493–673 K) and frequency dependence, as shown in Fig. 8(a), with exceptionally high low-frequency values ($\sim 10^7$) comparable to advanced lithium-based dielectrics ($\varepsilon' \approx 10^4$ at 493 K/50 Hz),[72] suggesting strong potential for energy storage applications. The characteristic ε' decrease with rising frequency reflects polarization relaxation dynamics, where dipolar and interfacial mechanisms dominant at low frequencies become unable to follow the rapidly oscillating field,[73] while the temperature-driven ε' enhancement indicates thermally activated polarization processes. Four primary mechanisms govern this behavior: electronic and ionic polarization at high frequencies, and dipolar/interfacial polarization at low frequencies,[74] with the latter diminishing as increasing

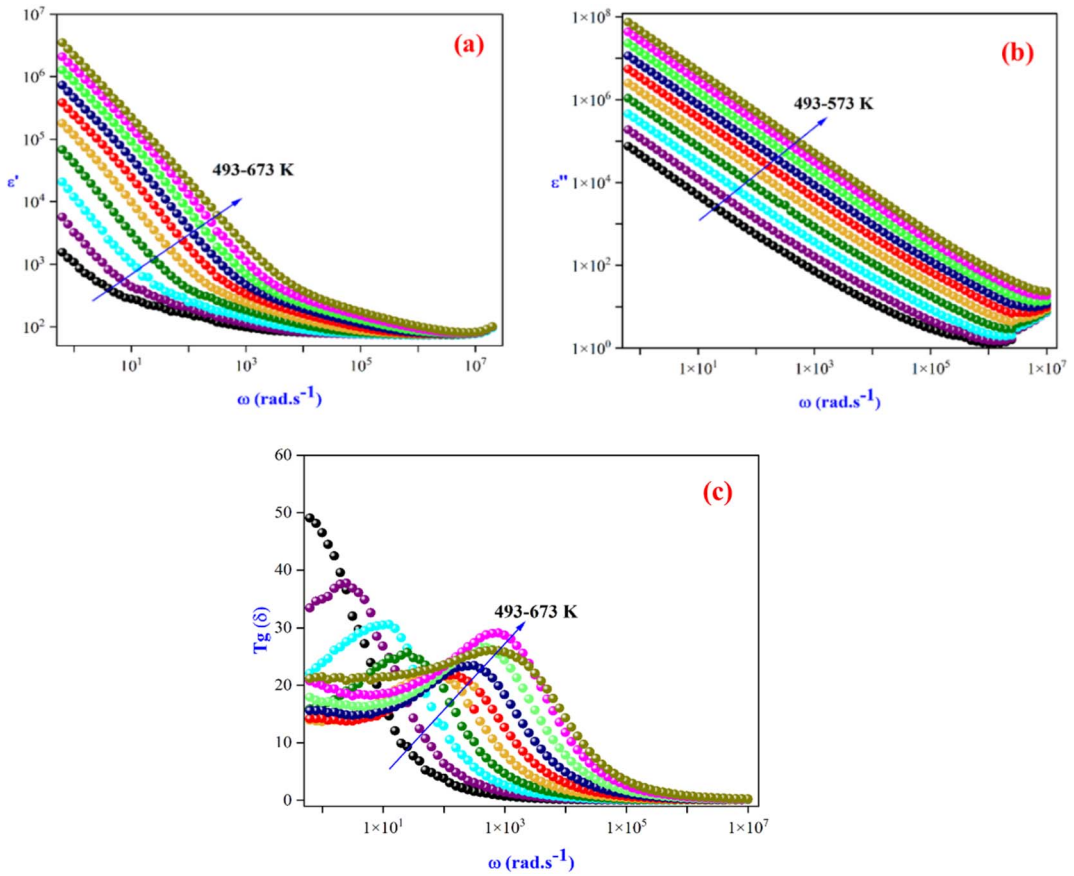

Fig. 8 (a) Frequency-dependent of real part of dielectric constants (ε'), (b) imaginary part (ε'') and (c) tan(δ) at different temperatures of $Li_3Mg_2NbO_6$.

frequency prevents dipole alignment, causing ε' to stabilize at interfacial polarization-dominated values.[75] The material's high ε' and tunable response, particularly in lithium-containing compounds, demonstrates excellent electric field resistance and promising performance for electronic storage systems,[76] with frequency- and temperature-dependent characteristics offering optimization pathways for specific applications ranging from high-capacity energy storage to high-frequency electronics.

As illustrated in Fig. 8(b), ε'' rises with temperature, particularly at lower frequencies, due to space charge polarization, resulting in elevated dielectric losses.[77] Consequently, tan δ is anticipated to mirror this pattern, with higher values at low frequencies and higher temperatures, driven by increased energy dissipation from interfacial charge buildup and dipole relaxation. At elevated frequencies, both ε'' and tan δ drop considerably, reflecting lower energy losses as charge carriers fail to keep pace with the fast-changing electric field, aligning with observed reductions in capacitance and resistivity (Fig. 8(c)). Capacitance data in Fig. 9 reinforce this trend, revealing higher capacitance at lower frequencies, with values increasing at higher temperatures due to enhanced ionic movement and weakened bond energies.[78] This relationship among dielectric constant, loss tangent, and capacitance highlights $Li_3Mg_2NbO_6$'s potential for high-frequency applications requiring minimal dielectric loss (low tan δ), while its temperature-sensitive properties enable adaptability for devices operating under varying thermal conditions.[79,80] The material's ordered rock-salt crystal structure, combined with the ability to adjust its composition through methods like Sn^{4+} doping, allows for fine-tuning of these dielectric properties, optimizing the balance between high capacitance and low loss for enhanced performance in microwave resonators and thermally stable capacitors.

3.2.4. Modulus study. To investigate the relaxation mechanisms in $Li_3Mg_2NbO_6$, the electric modulus formalism was employed, offering a clearer perspective on charge carrier dynamics by reducing the influence of electrode polarization.[81] The imaginary component of the electric modulus, $M''(\omega)$, displayed distinct frequency-dependent behavior (Fig. 10). At low frequencies, the absence of a peak suggests long-range charge carrier migration, facilitating unrestricted hopping between lattice sites.[82] Conversely, a prominent peak emerged at higher frequencies, indicating a shift to localized motion where carriers are confined within potential barriers or defect sites. The asymmetric broadening of these peaks confirms non-Debye relaxation behavior, implying a spectrum of relaxation times rather than a single dominant process.[83] As temperature increased, the M'' peaks shifted toward higher frequencies, consistent with thermally assisted hopping that accelerates relaxation and enhances carrier mobility.

From an Arrhenius analysis of the peak frequencies (Fig. 11), the activation energy (E_a) was calculated as 1.16 eV, closely matching the value obtained from DC conductivity measurements. This agreement suggests that ionic relaxation and

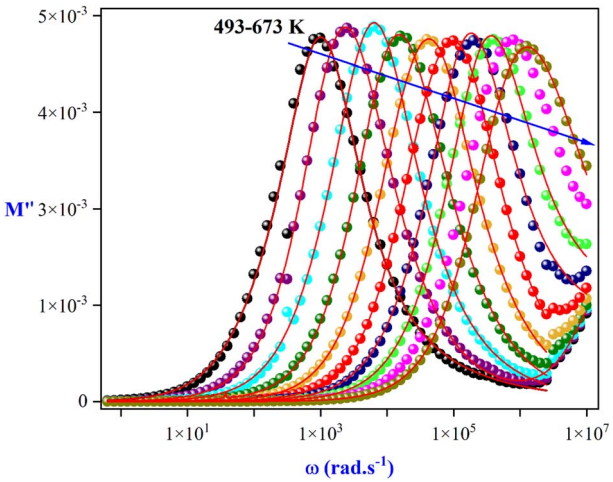

Fig. 10 Frequency dependence of the imaginary part of electric modulus at different temperatures.

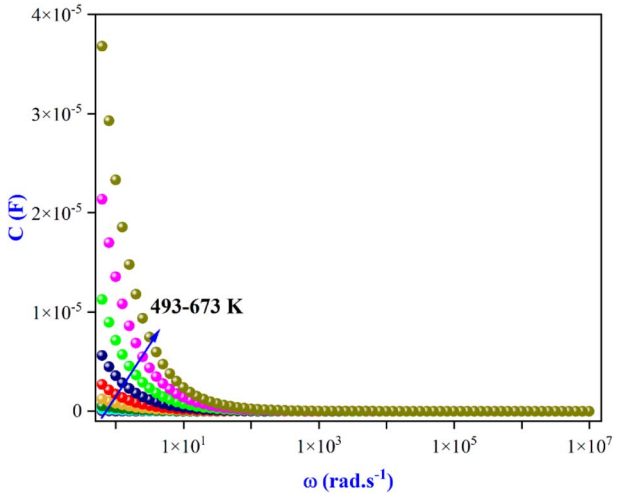

Fig. 9 The variation of capacity (C) as a function of frequency at different temperatures.

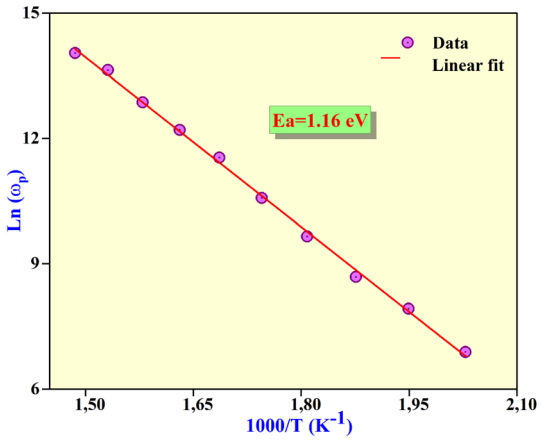

Fig. 11 Dependence of ln(ω_p) *versus* reciprocal temperature for $Li_3Mg_2NbO_6$.

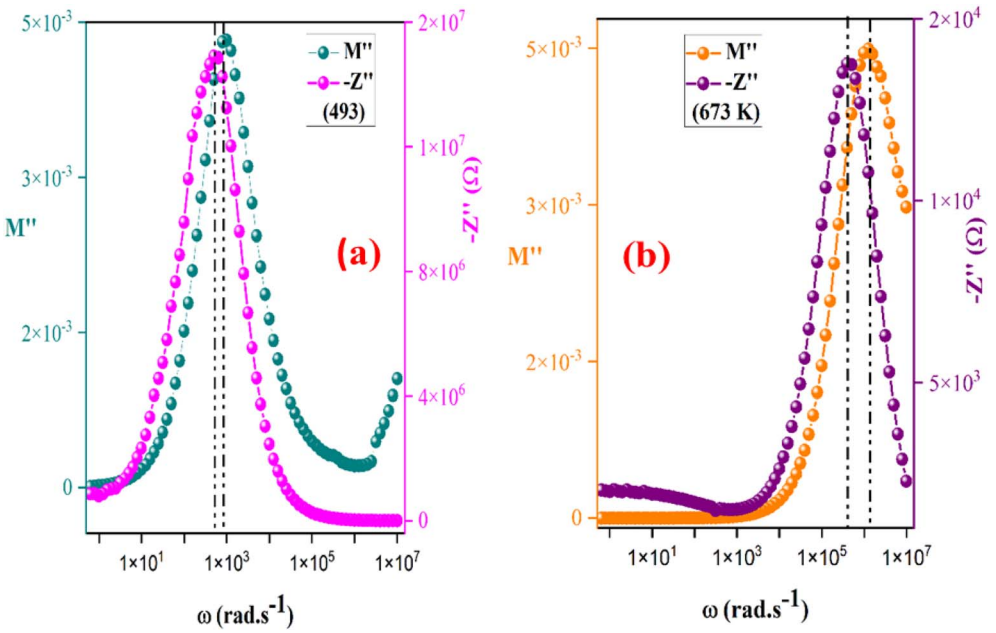

Fig. 12 Combined M'' and $-Z''$ spectroscopic plots at (a) 493 K and (b) 673 K.

charge transport in $Li_3Mg_2NbO_6$ are governed by the same thermally activated hopping mechanism.[84]

Further correlation with impedance spectroscopy (Fig. 12) revealed additional details about the relaxation process. At lower temperatures (493 K), the mismatch between Z'' and M'' peak positions indicates contributions from both localized and long-range charge dynamics, likely influenced by grain boundary effects. At elevated temperatures (673 K), the convergence of these peaks points to a transition toward localized hopping as the dominant relaxation mechanism.[85]

These findings demonstrate that dielectric relaxation in $Li_3Mg_2NbO_6$ is driven by thermally activated charge carriers, evolving from extended-range conduction at low frequencies to confined motion at higher frequencies. The non-Debye characteristics and consistent activation energy highlight the intrinsic connection between relaxation and conduction processes, shaped by the material's rock-salt layered structure and space charge interactions. Such insights are crucial for optimizing $Li_3Mg_2NbO_6$ in applications like microwave resonators and capacitors, where precise control over dielectric response and loss minimization are key to performance and stability.

3.3. Optical properties

Ultraviolet-visible (UV-Vis) spectroscopy offers a powerful, non-invasive approach to probe the optical characteristics of semiconductors, particularly complex oxides like $Li_3Mg_2NbO_6$, which contain lithium and exhibit intricate electronic structures. This technique yields critical insights into the material's photophysical properties without compromising sample integrity, making it ideal for comprehensive characterization alongside electrical and structural studies. The optical response of $Li_3Mg_2NbO_6$ is primarily dictated by its optical energy bandgap (E_g), a pivotal parameter that governs its suitability for applications in optoelectronics and photocatalysis. Room-temperature UV-Vis absorption spectra, collected over the 200–800 nm range (Fig. 13(a)), display four distinct absorption peaks at approximately 475, 500, 550, and 750 nm, each linked to specific electronic transitions within the material's lattice. The peaks at longer wavelengths (550 and 750 nm) are attributed to ligand-to-metal charge-transfer (LMCT) transitions within $[NbO_6]$ octahedral clusters, where electrons shift from oxygen 2p orbitals to unoccupied niobium 4d orbitals, highlighting the covalent nature of Nb–O bonds in these polyhedral units. In contrast, the shorter-wavelength peaks at 475 and 500 nm are associated with electronic transitions involving Li^+ and Mg^{2+} cations, likely arising from crystal-field-induced d–d transitions or interionic charge-transfer processes shaped by the unique coordination environments within the layered rock-salt structure of $Li_3Mg_2NbO_6$.

The optical bandgap was determined using the Tauc formalism, expressed as:[86]

$$(\alpha h\nu)^n = A(h\nu - E_g)$$

where α represents the absorption coefficient, $h\nu$ is the photon energy, A is a material-specific constant, and n indicates the transition type ($n = 1/2$ for direct allowed transitions, $n = 2$ for indirect allowed transitions). By constructing a Tauc plot and extrapolating the linear region of $(\alpha h\nu)^{(1/n)}$ *versus* $h\nu$ to the energy axis (Fig. 13(b)), a direct bandgap of 3.78 eV was calculated. This wide bandgap classifies $Li_3Mg_2NbO_6$ as a semiconductor comparable to other lithium-containing oxides, rendering it promising for applications such as UV photodetectors, transparent conductive films, and short-wavelength optoelectronic devices. The bandgap, slightly narrower than some lithium-based analogs, may reflect band-filling effects due

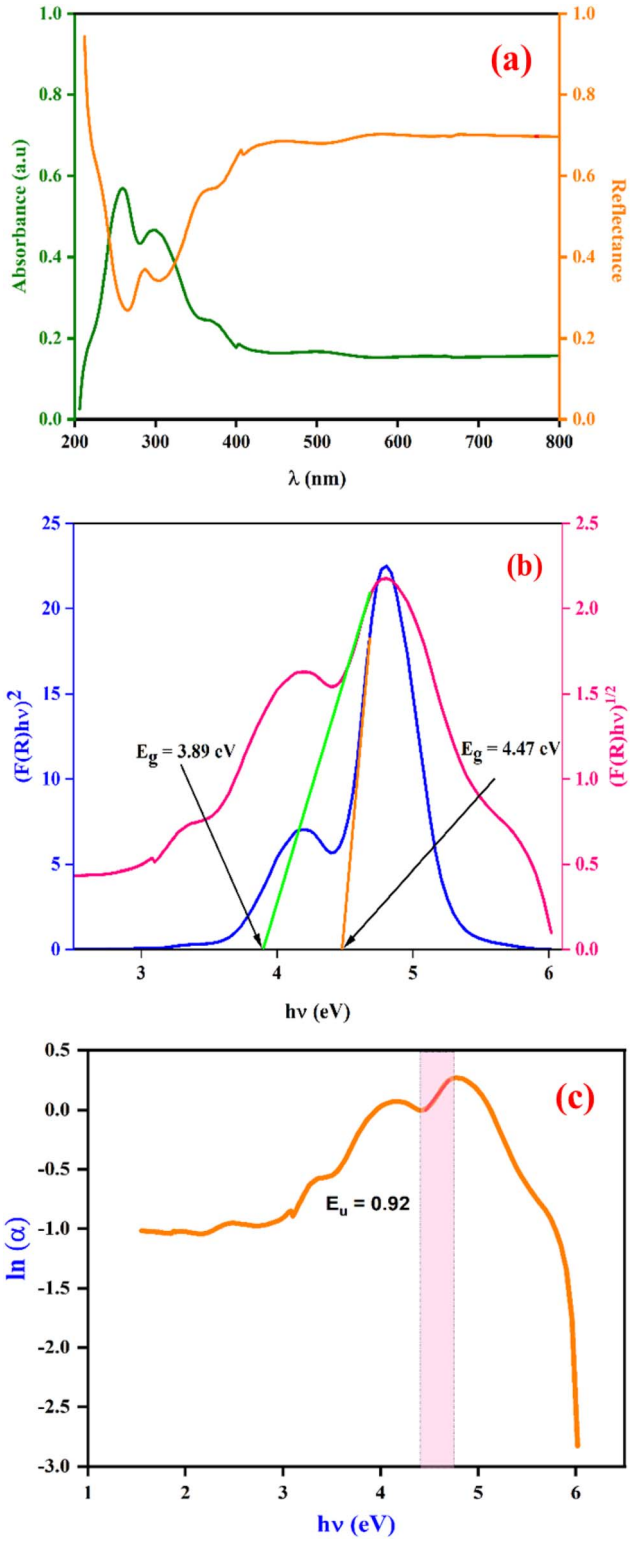

Fig. 13 (a) The UV-visible absorbance spectrum, (b) direct and indirect band gap, (c) ln(α) as a function of photon energy (eV) for $Li_3Mg_2NbO_6$ sample.

to intrinsic defects or subtle variations in cationic ordering within the rock-salt lattice. Importantly, the 3.78 eV bandgap surpasses the 1.23 eV threshold required for photoelectrochemical water splitting, suggesting potential for solar-driven hydrogen production, pending further evaluation of charge carrier dynamics and surface catalytic properties.

To quantify structural disorder and defect states, the Urbach energy (E_u) was analyzed, which characterizes the exponential tail near the absorption edge according to ref. 87:

$$\alpha = \alpha_0 \exp\left(\frac{h\nu - E_g}{E_u}\right) \quad (11)$$

where α_0 is a constant and E_u represents the Urbach energy in electronvolts. By plotting ln(α) against $h\nu$ (Fig. 13(c)) and extracting the inverse slope of the linear segment, an Urbach energy of 0.92 eV was determined, equivalent to approximately 24% of the bandgap. This substantial E_u value indicates a high density of localized subgap states, likely stemming from point defects (*e.g.*, oxygen vacancies), lattice distortions, or compositional inhomogeneities within the $Li_3Mg_2NbO_6$ structure. These disorder-induced states significantly influence charge carrier trapping, recombination kinetics, and space-charge polarization, thereby affecting both optical and electrical performance.[88]

The optical properties elucidated through UV-Vis spectroscopy provide a critical link to the electrical behavior observed in impedance and modulus spectroscopy studies. The localized states identified by the Urbach energy contribute to the distributed relaxation times observed in dielectric measurements, facilitating charge hopping and space-charge effects that underpin frequency- and temperature-dependent relaxation phenomena. Additionally, the LMCT transitions within [NbO_6] clusters, which dominate the absorption spectra, shape the electronic structure that governs ionic conduction pathways and dielectric losses. This interdependence underscores the complex defect chemistry of $Li_3Mg_2NbO_6$, where the ordered rock-salt framework, with its alternating Li^+, Mg^{2+}, and Nb^{5+} cations, modulates both optical absorption and charge transport.

The wide bandgap and significant Urbach energy highlight LMN's potential for specialized applications while also revealing challenges posed by its inherent disorder. The material's optical characteristics suggest viability for UV-sensitive devices and photocatalytic systems, but the high density of defect states may limit charge carrier mobility or increase recombination losses, necessitating targeted optimization. Defect engineering, such as doping with transition metals (*e.g.*, Sn^{4+}) or adjusting the Li/Mg ratio, could reduce subgap states or tune the bandgap to enhance optical transparency or catalytic efficiency. The structural similarity of $Li_3Mg_2NbO_6$ to other high-performance oxides, such as $Li_3Mg_2NbO_6$, invites comparative studies to uncover universal principles for designing wide-bandgap ceramics. Advanced synthesis techniques, including high-pressure sintering or controlled annealing, could further minimize disorder, improving the material's functional properties. These findings establish LMN as a versatile platform for optoelectronic devices, photocatalysts, and microwave dielectrics, where precise control of optical and electrical properties is paramount.[89] Future research should focus on correlating optical parameters with structural

modifications, exploring the material's performance under operational conditions, and integrating it into prototype devices to fully realize its technological potential.

In conclusion, UV-Vis spectroscopy of our sample reveals a complex interplay of electronic transitions, a wide 3.78 eV bandgap, and significant structural disorder, providing a comprehensive understanding of its photophysical and electrical properties. These insights, combined with electrical characterizations, offer a robust framework for tailoring the material's performance through defect control and compositional tuning, paving the way for its integration into advanced functional devices.

Taken together, the structural, optical, and electrical analyses reveal that the exceptional dielectric behavior of $Li_3Mg_2NbO_6$ arises from the synergistic interplay of its intrinsic characteristics. The orthorhombic rock-salt-derived lattice ensures a highly ordered ionic arrangement, minimizing defects and promoting uniform dipolar alignment, which underpins low dielectric loss and stable permittivity. The wide optical bandgap (~3.78 eV) effectively suppresses electronic polarization at microwave frequencies, while shallow defect states modulate space-charge polarization, influencing the frequency-dependent dielectric response. Electrical analysis further indicates thermally activated relaxation processes governed by ionic mobility and lattice vibrations, directly affecting dielectric stability under operational conditions. Together, these properties elucidate the fundamental mechanisms controlling LMN's low-loss, high-stability dielectric behavior, confirming its strong potential for microwave and energy storage applications.

4. Conclusion

$Li_3Mg_2NbO_6$ has been established as a multifunctional dielectric ceramic that integrates robust structural, electrical, and optical performance. The rock-salt-derived orthorhombic framework endows the material with high permittivity, low dielectric losses, and a wide direct bandgap of 3.78 eV, signifying its suitability for both microwave and UV optoelectronic applications. Electrical investigations reveal non-Debye relaxation and thermally activated charge transport ($E_a \approx 1.16$ eV), highlighting the influence of cation distribution and structural disorder on the conduction process. These insights underscore the potential of defect engineering, compositional substitution, and sintering optimization as effective routes to tailor its functional behavior. The combined dielectric, optical, and electrical characteristics position $Li_3Mg_2NbO_6$ as a versatile candidate for high-frequency resonators, thermally stable capacitors, and photoelectronic components relevant to emerging 5G/6G and sustainable energy technologies.

This work therefore opens new opportunities for the design of next-generation multifunctional ceramics combining structural stability, dielectric reliability, and optical responsiveness.

Author contributions

Samia Aydi: investigation, data curation, formal analysis, visualization, writing – original draft, writing – review & editing. Mohamed Mounir Bouzayani: investigation, data curation, formal analysis, visualization, writing – original draft, writing – review & editing. Moufida Boukriba: investigation, data curation, formal analysis, visualization, writing – original draft, writing – review & editing. Saber Nasri: supervision, resources, validation, methodology, writing – review & editing. Omar Radhi Alzoubi: investigation, formal analysis, visualization, writing – original draft, writing – review & editing. Abderrazek Oueslati: conceptualization, methodology, formal analysis, validation, writing – review & editing, project administration.

Conflicts of interest

The authors declare that they have no known competing financial interests or personal relationships that could have appeared to influence the work reported in this paper.

Data availability

The authors confirm that the data supporting the findings of this study are available from the corresponding author upon reasonable request.

Acknowledgements

The authors extend their appreciation to Umm Al-Qura University, Saudi Arabia for funding this research work through grant number: 25UQU4360914GSSR01.

References

1 Q. W. Liao, L. X. Li, X. Ren, X. X. Yu, D. Guo and M. J. Wang, *J. Am. Ceram. Soc.*, 2012, **95**, 3363.
2 C. S. Chen, C. C. Chou, C. S. Chen and I. N. Lin, *J. Eur. Ceram. Soc.*, 2004, **24**, 1795.
3 D. Zou, Q. L. Zhang, H. Yang and S. C. Li, *J. Eur. Ceram. Soc.*, 2008, **28**, 2777.
4 C. Liu, H. Zhang, G. Wang, T. Zhou, H. Su, L. Jia, L. Jin, J. Li and Y. Liao, *Mater. Res. Bull.*, 2017, **93**, 16.
5 M. Guo, S. P. Gong, G. Dou and D. X. Zhou, *J. Alloys Compd.*, 2011, **509**, 5988.
6 G. G. Yao, P. Liu and H. W. Zhang, *J. Am. Ceram. Soc.*, 2013, **96**, 1691.
7 W. Wersing, *Curr. Opin. Solid State Mater. Sci.*, 1996, **1**, 715.
8 M. T. Sebastian and H. Jantunen, *Int. Mater. Rev.*, 2008, **53**, 57.
9 S. J. Fiedziuszko, I. C. Hunter, T. Itoh, Y. Kobayashi, T. Nishikawa, S. N. Stitzer and K. Wakino, *IEEE Trans. Microwave Theory Tech.*, 2002, **50**, 706.
10 Y. L. Liao, F. Xu, D. N. Zhang, T. C. Zhou, Q. Wang, X. Y. Wang, L. J. Jia, J. Li, H. Su, Z. Y. Zhong and H. W. Zhang, *J. Am. Ceram. Soc.*, 2015, **98**, 2556.
11 H. Ren, L. Hao, H. Peng, *et al.*, *J. Eur. Ceram. Soc.*, 2018, **38**, 3498.
12 X. Lu, Y. Zheng, Z. Dong, *et al.*, *Mater. Lett.*, 2014, **131**, 1.
13 H. Ren, S. Jiang, M. Dang, *et al.*, *J. Alloys Compd.*, 2018, **740**, 1188.

14 L. L. Yuan and J. J. Bian, *Ferroelectrics*, 2009, **387**, 123.
15 P. Zhang, X. Zhao and Y. Zhao, *J. Mater. Sci.: Mater. Electron.*, 2016, **27**, 6395.
16 Y. Qian, Q. Zhang, X. Tang, *et al.*, *J. Mater. Sci.: Mater. Electron.*, 2021, **32**, 22450.
17 P. Zhang, Y. G. Zhao and L. X. Li, *Phys. Chem. Chem. Phys.*, 2015, **17**, 16692.
18 V. B. Braginsky, V. S. Ilchenko and K. S. Bagdassarov, *Phys. Lett. A*, 1987, **120**, 300.
19 V. L. Gurevich and A. K. Tagantsev, *Adv. Phys.*, 1991, **40**, 719.
20 J. D. Breeze, J. M. Perkins, D. W. McComb and N. M. Alford, *J. Am. Ceram. Soc.*, 2009, **92**, 671.
21 J. Guo, D. Zhou, H. Wang and X. Yao, *J. Alloys Compd.*, 2011, **509**, 5863.
22 S. George and M. T. Sebastian, *Int. J. Appl. Ceram. Technol.*, 2011, **8**, 1400.
23 T. Zhang and R. Zuo, *Ceram. Int.*, 2014, **40**, 15677.
24 G. Wang, H. Zhang, C. Liu, *et al.*, *J. Electron. Mater.*, 2018, **47**, 4672.
25 P. Zhang, H. Xie, Y. Zhao, *et al.*, *J. Alloys Compd.*, 2017, **690**, 688.
26 X. Zhou, X. Ning, X. Zhang, *et al.*, *J. Mater. Sci.: Mater. Electron.*, 2020, **31**, 17029.
27 M. T. Sebastian and H. Jantunen, *Int. Mater. Rev.*, 2008, **53**, 57.
28 D. Zhou, D. Guo, W. B. Li, L. X. Pang, X. Yao, D. W. Wang and I. M. Reaney, *J. Mater. Chem. C*, 2016, **4**, 5357.
29 D. Zhou, W. B. Li, H. H. Xi, L. X. Pang and G. S. Pang, *J. Mater. Chem. C*, 2015, **3**, 2582.
30 R. I. Scott, M. Thomas and C. Hampson, *J. Eur. Ceram. Soc.*, 2003, **23**, 2467.
31 B. Jancar, M. Valant and D. Suvorov, *Chem. Mater.*, 2004, **16**, 1075.
32 G. K. Choi, J. R. Kim, S. H. Yoon and K. S. Hong, *J. Eur. Ceram. Soc.*, 2007, **27**, 3063.
33 D. Zhou, L. X. Pang, J. Guo, Z. M. Qi, T. Shao, X. Yao and C. A. Randall, *J. Mater. Chem.*, 2012, **22**, 21412.
34 L. Fang, Y. Tang, D. Chu, *et al.*, *J. Mater. Sci.: Mater. Electron.*, 2012, **23**, 478.
35 G. Wang, H. Zhang, X. Huang, *et al.*, *Ceram. Int.*, 2018, **44**, 19295.
36 G. Wang, H. Zhang, C. Liu, *et al.*, *Mater. Lett.*, 2018, **217**, 48.
37 W. Wang, C. Liu, L. Shi, *et al.*, *Appl. Phys. A: Mater. Sci. Process.*, 2019, **125**, 1.
38 G. Wang, D. Zhang, Y. Lai, *et al.*, *J. Alloys Compd.*, 2019, **782**, 370.
39 P. Zhang, L. Liu, Y. Zhao, *et al.*, *J. Mater. Sci.: Mater. Electron.*, 2017, **28**, 5802.
40 P. Zhang, J. Liao, Y. Zhao, *et al.*, *J. Mater. Sci.: Mater. Electron.*, 2017, **28**, 686690.
41 D. W. Kim, D. K. Kwon, S. H. Yoon and K. S. Hong, *J. Am. Ceram. Soc.*, 2006, **89**, 3861.
42 D. Zhou, H. Wang and X. Yao, *Mater. Chem. Phys.*, 2007, **104**, 397.
43 C. L. Huang and M. H. Weng, *Mater. Lett.*, 2000, **43**, 32.
44 S. H. Yoon, D. W. Kim, S. Y. Cho and K. S. Hong, *J. Eur. Ceram. Soc.*, 2006, **26**, 2051.
45 Y. Wang, R. Zuo, C. Zhang, J. Zhang and T. Zhang, *J. Am. Ceram. Soc.*, 2015, **98**, 1.
46 L. X. Pang, H. Wang, D. Zhou and X. Yao, *J. Electroceram.*, 2009, **23**, 13.
47 E. S. Kim and D. H. Kang, *Ceram. Int.*, 2008, **34**, 883.
48 R. Jindal, M. M. Sinha and H. C. Gupta, *Spectrochim. Acta, Part A*, 2013, **113**, 286.
49 A. Watanabe, *J. Solid State Chem.*, 2000, **153**, 174.
50 D. Zhou, L. X. Pang, H. Wang, J. Guo, X. Yao and C. A. Randall, *J. Mater. Chem.*, 2011, **21**, 18412.
51 D. Zhou, L. X. Pang, J. Guo, Z. M. Qi, T. Shao, Q. P. Wang, H. D. Xie, X. Yao and C. A. Randall, *Inorg. Chem.*, 2014, **53**, 1048.
52 A. K. Bhattacharya, K. K. Mallick and A. Hartridge, *Mater. Lett.*, 1997, **30**, 7.
53 P. Zhang, S. Wu and M. Xiao, *J. Alloys Compd.*, 2018, **766**, 498.
54 A. Kudo, K. Omori and H. A. Kato, *J. Am. Chem. Soc.*, 1999, **121**, 11459–11467.
55 J. A. Baglio and O. J. Sovers, Crystal structures of the rare-earth orthovanadates, *J. Solid State Chem.*, 1971, **3**, 458.
56 S. A. Miller, H. H. Caspers and H. E. Rast, *Phys. Rev.*, 1968, **168**, 964.
57 M. Pollet and S. Maranel, *J. Eur. Ceram. Soc.*, 2003, **23**, 1925.
58 R. F. Moran, A. Fernandes, D. M. Dawson, S. Sneddon, A. S. Gandy, N. Reeves-McLaren, K. R. Whittle and S. E. Ashbrook, *J. Phys. Chem. C*, 2020, **124**, 17073.
59 N. Xu, J. Zhou, H. Yang, *et al.*, *Ceram. Int.*, 2014, **40**, 15191.
60 J. Zhang, Z. Yue, X. Zhang, *et al.*, *Ceram. Int.*, 2015, **41**, S515.
61 R. Zuo, H. Qi, F. Qin and Q. Dai, *J. Eur. Ceram. Soc.*, 2018, **38**, 5442.
62 S. Zhai, P. Liu, Z. Fu, *et al.*, *J. Mater. Sci.: Mater. Electron.*, 2019, **30**, 5404.
63 W. Xia, L. Li, P. Zhang, *et al.*, *Mater. Lett.*, 2011, **65**, 3317.
64 Z. Fu, X. Chen, Y. Zhang, *et al.*, *Ceram. Int.*, 2022, **48**, 36638.
65 R. D. Shannon, *J. Appl. Phys.*, 1993, **73**, 348.
66 Y. Lai, H. Su, G. Wang, *et al.*, *J. Am. Ceram. Soc.*, 2019, **102**, 1893.
67 Y. Lai, C. Hong, L. Jin, X. Tang, H. Zhang, X. Huang, J. Li and H. Su, *Ceram. Int.*, 2017, **43**, 16167.
68 J. Ma, Z. Fu, P. Liu, *et al.*, *Mater. Sci. Eng., B*, 2016, **204**, 15.
69 R. Vali, *Solid State Commun.*, 2009, **149**, 1637.
70 F. D. Hardcastle and I. E. Wachs, *J. Phys. Chem.*, 1991, **95**, 5031.
71 Y. Lai, C. Hong, L. Jin, X. Tang, H. Zhang, X. Huang, J. Li and H. Su, *Ceram. Int.*, 2017, **43**, 16167.
72 R. D. Shannon, *J. Appl. Phys.*, 1993, **73**, 348.
73 J. Petzelt and S. Kamba, *Mater. Chem. Phys.*, 2003, **79**, 175.
74 D. Zhou, H. Wang, Q. P. Wang, X. G. Wu, J. Guo, G. Q. Zhang, L. Shui, X. Yao, C. A. Randall, L. X. Pang and H. C. Liu, *Mater. Lett.*, 2010, **3**, 253.
75 A. J. Bosman and E. E. Havinga, *Phys. Rev.*, 1963, **129**, 1593.
76 L. L. Yuan and J. J. Bian, *Ferroelectrics*, 2009, **387**, 123.
77 L. X. Pang, H. Wang, D. Zhou and X. Yao, *J. Alloys Compd.*, 2010, **493**, 626.
78 D. Zhou, H. Wang, L.-X. Pang, X. Yao and X.-G. Wu, *J. Am. Ceram. Soc.*, 2008, **91**, 4115.

79 X. M. Chen, Y. Xiao, X. Q. Liu and X. Hu, *J. Electroceram.*, 2003, **10**, 111.
80 H.-C. Huang; Y. Wang and X. Jian, *Asia-Pacific Conference on Antennas and Propagation (APCAP)*, 2018, p. 420.
81 C. Pecharroman, M. Ocana, P. Tartaj and C. J. Serna, *Mater. Res. Bull.*, 1994, **29**, 417.
82 E. Kobayashi, L. S. Plashnitsa, T. Doi, S. Okada and J. I. Yamaki, *Electrochem. Commun.*, 2010, **12**, 894.
83 A. Rossbach, F. Tietz and S. Grieshammer, *J. Power Sources*, 2018, **391**, 1.
84 A. R. Armstrong, M. Holzapfel, P. Novák, C. S. Johnson, S.-H. Kang, M. M. Thackeray and P. G. Bruce, *J. Am. Chem. Soc.*, 2006, **128**, 8694.
85 M. Sathiya, A. M. Abakumov, D. Foix, G. Rousse, K. Ramesha, M. Saubanère, M. L. Doublet, H. Vezin, C. P. Laisa, A. S. Prakash, D. Gonbeau, G. Van Tendeloo and J.-M. Tarascon, *Nat. Mater.*, 2015, **14**, 230; I. P. Kondratyuk, B. A. Maksimov and L. A. Muradyan, *Dokl. Akad. Nauk SSSR*, 1987, **292**, 1376.
86 A. B. Bykov, A. P. Chirkin, L. N. Demyanets, S. N. Doronin, E. A. Genkina, A. K. Ivanov-Shits, I. P. Kondratyuk, B. A. Maksimov, O. K. Mel'nikov, L. N. Muradyan, V. I. Simonov and V. A. Timofeeva, *Solid State Ionics*, 1990, **38**, 31.
87 S. A. Anna, B. Kalska, P. Jönsson, L. Häggström, P. Nordblad, R. Tellgren and J. Thomas, *J. Mater. Chem.*, 2000, **10**, 2542.
88 H. Karami and F. Taala, *J. Power Sources*, 2011, **196**, 6400.
89 M. Sato, S. Tajimi, H. Okawa, K. Uematsu and K. Toda, *Solid State Ionics*, 2002, **152**, 247.